

**AD-A265 214**



**WL-TR-93-3002**



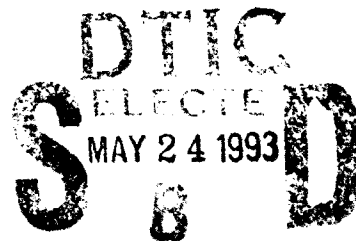
**CALCULATIONS ON UNSTEADY TYPE IV INTERACTION AT  
MACH 8**

**Datta Gaitonde  
Universal Energy Systems  
4401 Dayton-Xenia Road  
Dayton, OH 45432**

**January 1993**

**Final Report for Period December 1991 - August 1992**

**Approved for public release; distribution is unlimited.**



**FLIGHT DYNAMICS DIRECTORATE  
WRIGHT LABORATORY  
AIR FORCE SYSTEMS COMMAND  
WRIGHT-PATTERSON AIR FORCE BASE, OHIO 45433-7913**

**93-11487**



**93 5**

**503**

**410p8**

# NOTICE

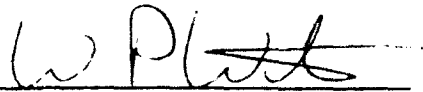
When Government drawings, specifications, or other data are used for any purpose other than in connection with a definitely Government-related procurement, the United States Government incurs no responsibility or any obligation whatsoever. The fact that the government may have formulated or in any way supplied the said drawings, specifications, or other data, is not to be regarded by implication, or otherwise in any manner construed, as licensing the holder, or any other person or corporation; or as conveying any rights or permission to manufacture, use, or sell any patented invention that may in any way be related thereto.

This report is releasable to the National Technical Information Service (NTIS). At NTIS, it will be available to the general public, including foreign nations.

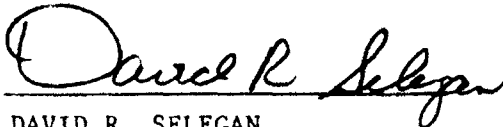
This technical report has been reviewed and is approved for publication.



DATTA GAITONDE  
Visiting Scientist



W. PHILLIP WEBSTER  
Technical Manager  
CFD Research Section



DAVID R. SELEGAN  
Chief  
Aeromechanics Division

If your address has changed, if you wish to be removed from our mailing list, or if the addressee is no longer employed by your organization please notify WL/FIMC, WPAFB, OH 45433-7913 to help us maintain a current mailing list.

Copies of this report should not be returned unless return is required by security considerations, contractual obligations, or notice on a specific document.

REPORT DOCUMENTATION PAGE			Form Approved OMB No 0704-0188	
<small>Public reporting burden for this collection of information is estimated to average 1 hour per response, including the time for reviewing instructions, searching existing data sources, gathering and maintaining the data needed, and completing and reviewing the collection of information. Send comments regarding this burden estimate or any other aspect of this collection of information, including suggestions for reducing this burden, to Washington Headquarters Services, Directorate for Information Operations and Reports, 1215 Jefferson Davis Highway, Suite 1204, Arlington, VA 22202-4302, and to the Office of Management and Budget, Paperwork Reduction Project (0704-0188), Washington, DC 20503.</small>				
1. AGENCY USE ONLY (Leave blank)	2. REPORT DATE Jan 93	3. REPORT TYPE AND DATES COVERED Final Report, Dec 91 to Aug 92		
4. TITLE AND SUBTITLE Calculations on Unsteady Type IV Interaction at Mach 8		5. FUNDING NUMBERS F33615-90-C-2089 PE- 62203 PR-2307 TA-N6 WU-7		
6. AUTHOR(S) Datta Gaitonde				
7. PERFORMING ORGANIZATION NAME(S) AND ADDRESS(ES) Universal Energy Systems, Inc. 4401 Dayton-Xenia Road Dayton OH 45432		8. PERFORMING ORGANIZATION REPORT NUMBER		
9. SPONSORING/MONITORING AGENCY NAME(S) AND ADDRESS(ES) Flight Dynamics Directorate Wright Laboratory (WL/FIM JOSEPH SHANG 513-255-6156) Air Force Materiel Command Wright-Patterson AFB OH 45433-7913		10. SPONSORING/MONITORING AGENCY REPORT NUMBER WL-TR-93-3002		
11. SUPPLEMENTARY NOTES				
12a. DISTRIBUTION / AVAILABILITY STATEMENT Approved for public release; distribution is unlimited.		12b. DISTRIBUTION CODE		
13. ABSTRACT (Maximum 200 words) The viscous unsteady flow due to a Type IV shock-on-shock interaction at Mach 8 is examined with an implicit flux-split scheme. A sequence of grids is utilized to perform a grid resolution study and the results are compared with experimental values. The formulation is finite-volume with higher order accuracy obtained with the MUSCL approach in conjunction with a limiter to prevent oscillations. Viscous terms are centrally differenced. The flow exhibits a limit cycle in aggregate quantities which can be related to the details for the flow structure. The supersonic jet bounded by the two shear layers displays large scale movement at a dominant frequency of 32 kHz. This is accompanied by variation in the angle between the terminating jet bow shock and the surface tangent. Unsteady separation regions are observed both above and below the point of jet impingement.				
14. SUBJECT TERMS Hypersonic, high-speed, Type IV Interaction Flux-splitting, upwinding, implicit, unsteady		15. NUMBER OF PAGES 41		16. PRICE CODE
17. SECURITY CLASSIFICATION OF REPORT Unclassified	18. SECURITY CLASSIFICATION OF THIS PAGE Unclassified	19. SECURITY CLASSIFICATION OF ABSTRACT Unclassified	20. LIMITATION OF ABSTRACT Unclassified	

# Contents

List of Figures . . . . .	iv
List of Tables . . . . .	v
Acknowledgements . . . . .	vi
1 Introduction . . . . .	1
2 Theoretical Model . . . . .	6
3 Boundary Conditions and Numerical Details . . . . .	9
4 Results . . . . .	10
5 Conclusions . . . . .	26
6 References . . . . .	27
Nomenclature . . . . .	31

DTIC QUALITY INSPECTED 5

Accession For	
NTIS GRA&I	<input checked="" type="checkbox"/>
DTIC TAB	<input type="checkbox"/>
Unannounced	<input type="checkbox"/>
Justification	
By	
Distribution/	
Availability Codes	
Dist	Avail and/or Special
A-1	

## List of Figures

1	Schematic of Type IV interference pattern . . . . .	2
2	Structure of grid employed . . . . .	11
3	Mach contours on coarse mesh . . . . .	12
4	Log residuals on Grid 2 Type IV interaction . . . . .	15
5	Comparison of implicit and explicit algorithm time histories on Grid 2 - Type IV interference . . . . .	17
6	Time history of Type IV interaction on Grid 3 . . . . .	18
7	Representative maximum surface loading cycles - Grid 3 Type IV interaction	20
8	Mach contours at various points in limit cycle - Grid 3 Type IV interaction	21
9	Surface loading at various points in limit cycle - Grid 3 Type IV interaction	22

## List of Tables

1	Shock Interference Grid Details . . . . .	13
---	---	----

## **Acknowledgements**

Computations were performed on computers at WPAFB and the NAS program. The support and assistance of the staff at both locations are gratefully acknowledged.

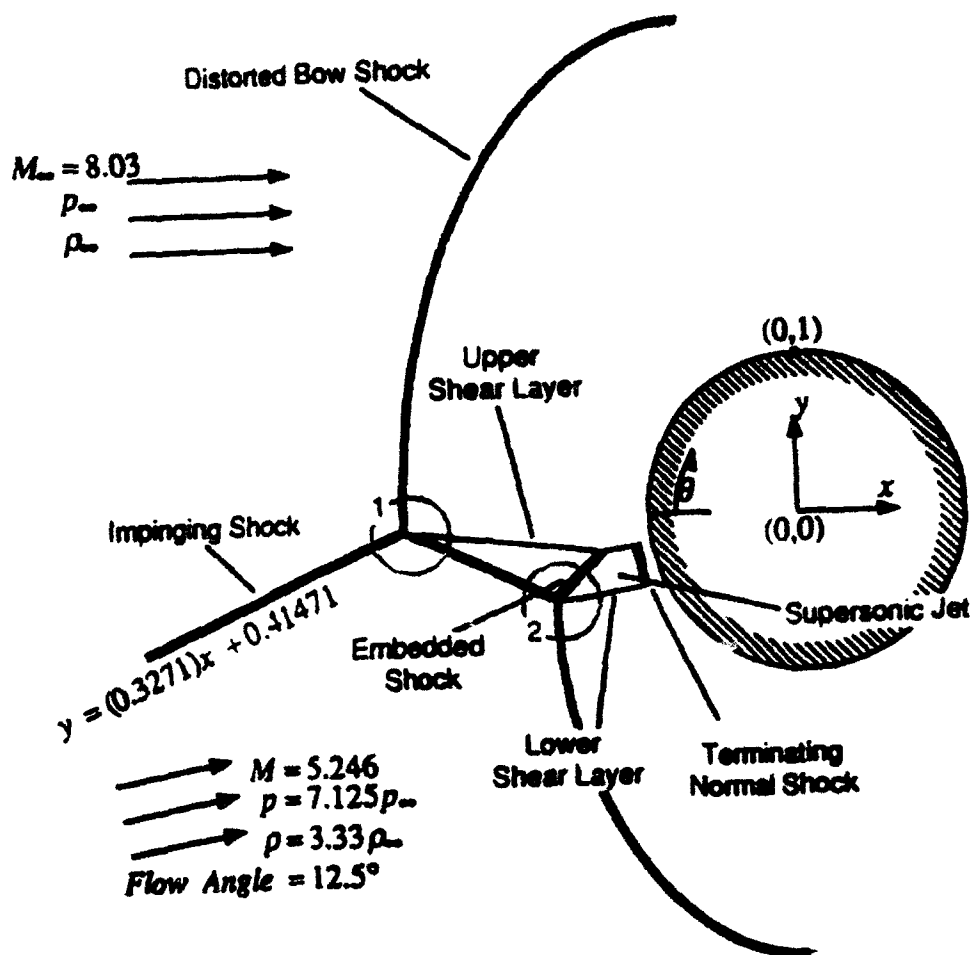
# 1. Introduction

A pacing item in the development of hypersonic vehicle design is the capability to accurately predict the heating on cowl-lips due to shock-on-shock interactions [1]. The forebodies of vehicles proposed for high speeds typically act as a compression system which facilitates optimum mass flow through the inlet. Depending upon the flight condition, the resultant system of forebody shocks may interact with the bow shock due to the cowl-lip of the inlet. The resulting interaction, often denoted "interference pattern," can lead to severe amplification of pressure and heat transfer on the cowl-lip. This may have catastrophic consequences for the vehicle unless accounted for in the design.

Shock-on-shock interactions in the presence of a cowl-lip can result in a range of patterns depending primarily on the location of the intersection between the impinging and cowl shocks. Edney [2] classified these distinct interactions into six different categories: Types I to VI. The highest surface loading occurs in the Type IV interaction shown schematically in Figure 1. This pattern is obtained when the impinging shock intersects the nearly normal portion of the cowl bow shock. Two triple points are formed from which emanate two shear layers. The flow between these passes through a series of weak oblique shocks and expansion fans until the supersonic jet so formed strikes the surface of cylinder (or cowl-lip) after the formation of a terminating jet bow shock. The flow then expands on either side of the stagnation point. The jet impingement process results in the maximum augmentation of peak heat transfer and surface pressure.

Several studies have investigated shock-on-shock interactions at a range of free stream Mach numbers. Following the efforts of Edney, the problem has been addressed with both experimental [3-5] and theoretical efforts. Among the latter are the semi-empirical methods of Hains *et al.* [6], Morris *et al.* [7] and the graphical methods of Crawford [8] and Bramlette [9].





$$M_{\infty} = 8.03$$

$$\text{Cylinder Radius} = 1.5\text{in.}$$

$$T_{\infty} = 200.8R$$

$$T_{\text{wall}} = 530R$$

$$\text{Impinging shock angle} = 18.1^{\circ}$$

Figure 1: Schematic of Type IV interference pattern

Computational solutions with the Navier-Stokes equations have been reported by several researchers, including Tannehill *et al.* [10], White *et al.* [11], Klopfer *et al.* [12], Peery *et al.* [13], Moon *et al.* [14] and Thareja *et al.* [15]. These studies employ a range of numerical algorithms including finite-difference and finite-volume implementations of centered and characteristic-based schemes. In addition to providing a quantitative assessment of the amplification in surface loading, these solutions have advanced the understanding of the characteristics of shock-on-shock interactions. The resulting pattern, for example, has been shown to be very sensitive to the location of the point of intersection of the impinging and bow shocks.

One of the few unsteady calculations to date was reported by Klopfer *et al.* who examined the effect of varying the impinging shock location dynamically, as would be expected in a flight vehicle. As the impinging shock is moved from one extreme position to the other, all of the patterns of Edney were successively obtained. Nevertheless, a common underlying assumption in each of the above calculations has been that for a given location of the impinging shock, i.e., for a given interaction pattern, the flow is steady.

However, there is reason to believe that some Type IV interactions are unsteady. A concrete example is presented in Figure 1 which focuses on the Mach 8 Type IV interaction examined in this research. The impinging shock is created upstream by a wedge of  $15^\circ$  angle resulting in post-impinging shock flow of Mach 5.25. The cowl-lip is adequately simulated by a cylinder. This configuration was investigated experimentally by Wieting *et al.* [5] and has been examined in several computational studies in recent years.

Although the flow was assumed to be steady initially, Holden [16] suggests that unsteadiness in the frequency range between 3 to 10kHz is evident in surface loading experimental data. Indeed, several computational studies have noted a difficulty in obtaining converged results for Type IV interactions not only under the above conditions [12,13] but at higher Mach numbers [17] as well. However, no linkage was proposed between the unsteadiness in

aggregate quantities and coherent flow structures.

The first attempt at analyzing the details of the unsteady flow was performed by Kroll *et al.* [18]. Their research examined the interaction under inviscid conditions with a range of upwind and centered schemes. In a detailed study that included several time-accurate integration methods and degrees of mesh resolution, they simulated the unsteadiness of the interaction and related it to the coherent flow features. They concluded that the unsteady limit cycle consists of an oscillation of the terminating jet bow shock about a mean position. This is accompanied by attendant effects in the remainder of the flow. Further discussion of their results is presented in Chapter 4.

This inviscid analysis, while useful in characterizing the unsteadiness, fails to provide critically important information about thermal loading. Further, viscous effects are anticipated to be significant in the stagnation region in the close vicinity of the terminating jet bow shock. The impact of viscosity on the nature of the unsteadiness is not immediately evident. It is the principal purpose of this research to address these questions through numerical simulation.

In recent years, significant advances have been attained in the development of numerical schemes for the Euler equations. Unlike the centered schemes of Refs. [19-21], the newer schemes use upwind methods to obviate the need for explicit damping terms. These newer methods may be classified into the means by which higher order accuracy is attained MUSCL (Monotonic Upwind-Centered Scheme for Conservation Laws) or non-MUSCL. Examples of the former are the flux-vector split methods of Steger and Warming [22] and of van Leer [23] and the flux-difference split method of Roe [24]. Methods obtaining higher order accuracy with non-MUSCL methods include the "upwind" and "symmetric" TVD (Total Variation Diminishing) methods of Yee [25] and Harten and Yee [26], respectively.

Although preliminary calculations with the van Leer and Roe schemes are reported in this work, the principal method employed is that of MacCormack and Candler [27], denoted

as the **MC** method. A brief description is provided in Chapter 2 followed by a note on the boundary conditions and other numerical details (Chapter 3). Finally, the results are examined in Chapter 4 which includes an investigation of the effect of mesh resolution as well as of the time-accuracy of the algorithm.

## 2. Theoretical Model

The 2-D full Navier Stokes equations are solved in strong conservation form:

$$\frac{\partial \hat{U}}{\partial t} + \frac{\partial \hat{F}}{\partial \xi} + \frac{\partial \hat{G}}{\partial \eta} = 0 \quad (2.1)$$

The  $\xi$  coordinate lines wrap around the cylinder while the  $\eta$  lines are body-normal thus forming an orthogonal mesh. In Equation 2.1,  $\hat{U}$  is the solution vector of conserved variables ( $\hat{U} = \{\rho, \rho u, \rho v, \rho e\}/J$ ) while the flux vectors,  $\hat{F}$  and  $\hat{G}$  include the full viscous and inviscid terms. The perfect gas assumption is invoked, the molecular viscosity is approximated by Sutherland's law and the molecular Prandtl number  $Pr$  is assumed to be constant (0.73).

Equation 2.1 may be interpreted as describing the balance of mass, momentum and energy fluxes over an arbitrary control volume. With first-order Euler implicit time discretization and linearization of the fluxes in time, the discretized equation may be written in the form:

$$\{NUMERICS\} \delta \bar{U} = PHYSICS \quad (2.2)$$

where *PHYSICS* represents the residual, *NUMERICS* contains the driving terms and  $\delta \bar{U}$  denotes the change in the solution vector at each time step. The full Navier-Stokes equations are utilized in computing the residual with the appropriate upwind model for the inviscid terms. Viscous flux terms are centrally evaluated.

For simplicity, two assumptions are employed in evaluating the *NUMERICS* portion of Equation 2.2. First, the spatial differences in flux Jacobians are calculated with the first order spatially accurate Steger Warming method. This enhances the diagonal dominance property of Equation 2.2 [28] leading to a robust solution procedure as described below. Secondly, the thin layer approximation is employed for the viscous Jacobians resulting in a significant reduction of computational requirements.

Time integration is achieved with a residual driven line Gauss-Seidel relaxation scheme

as described in Ref. [29]. With this choice, Equation 2.2 represents a block tridiagonal system. The method is unconditionally stable for model diffusion and convection equations and is also known to be relatively insensitive to the choice of time increment per iteration [30]. The formal time-accuracy (first order) of the resultant algorithm is not affected by the simplifications described above. Nevertheless, the use of inconsistent differencing needs further study particularly since the *NUMERICS* portion employs first order spatial derivatives. A detailed analysis of the time accuracy of the method is deferred to Chapter 4.

A brief description of the spatial scheme is presented with reference to the evaluation of the Cartesian flux ( $\hat{G}$ ) at a  $j + \frac{1}{2}$  surface of the cell centered finite volume formulation. The extension to general coordinates is straightforward [31] as is the implementation of the viscous terms which are centered. At each interface, the state of the flow is described by two vectors of conserved variables,  $U^L$  and  $U^R$  on either side of the interface. These are obtained by upwind extrapolation to the cell surface with the MUSCL approach of van Leer [32] in conjunction with a limiter. With  $W$  denoting the vector of extrapolated quantities:

$$W_{j+\frac{1}{2}}^L = W_j + \frac{1}{2}\hat{\Delta}_{j+\frac{1}{2}}; \quad W_{j+\frac{1}{2}}^R = W_{j+1} - \frac{1}{2}\hat{\Delta}_{j+\frac{1}{2}} \quad (2.3)$$

where  $\hat{\Delta}$  introduces the limiter function,  $f$ :

$$\hat{\Delta}_{j+\frac{1}{2}} = f(\Delta_{j+\frac{1}{2}}, \Delta_{j-\frac{1}{2}}); \quad \Delta_{j+\frac{1}{2}} = W_{j+\frac{1}{2}}^R - W_{j+\frac{1}{2}}^L \quad (2.4)$$

In the present work the primitive variables ( $W = \{\rho, u, v, p\}$ ) are extrapolated and  $U$  is then reconstructed. The limiter  $f$ , preserves monotonicity within the solution. Many limiter functions have been proposed in the literature. The calculations in this work employ the *minmod* limiter [33] chosen for its popularity and robustness:

$$f(x, y) = \text{minmod}(x, y) = \text{sgn}(x) \cdot \max\{0, \min[|x|, y \cdot \text{sgn}(x)]\} \quad (2.5)$$

Following Steger *et al.* [22], the first order homogeneous hyperbolic property of the flux Jacobian  $B$ , ( $B = \partial G / \partial U$ ,  $G = BU$ ), is utilized to split the fluxes into positive and

negative components:

$$B = Q^{-1} \Lambda Q = Q^{-1} (\Lambda_+ + \Lambda_-) Q = B_+ + B_- \quad (2.6)$$

where  $\Lambda$  is a diagonal matrix consisting of the eigenvalues of  $B$ ,  $\Lambda = \text{diag} \{v, v + c, v - c\}$ .  $\Lambda_+$  and  $\Lambda_-$  denote the splitting of the eigenvalues into positive and negative components. At a face  $j + 1/2$ , therefore, the *original* Steger Warming (abbreviated **SW**) flux ( $G_{SW}$ ) may be written as:

$$G_{SW,j+\frac{1}{2}} = B_+^L U^L + B_-^R U^R \quad (2.7)$$

The inviscid flux formula of MacCormack and Candler [27] ( $G_{MC}$ ) reads:

$$G_{MC,j+\frac{1}{2}} = B_+^{\frac{L+R}{2}} U^L + B_-^{\frac{L+R}{2}} U^R \quad (2.8)$$

where  $U^L$  and  $U^R$  are evaluated with the MUSCL approximation (Eqns 2.3 and 2.4). The essential difference between the SW and the MC schemes is in the manner in which the flux Jacobians ( $B$ ) are evaluated. While SW employs upwinding for the Jacobians, MC is centered. Additional details of the MC method may be found in Ref. [34].

The MC scheme was developed for application only in the boundary layers, and in fact leads to instability when applied in regions of discontinuities such as shock waves. As a result, it is necessary to revert to the SW scheme near shocks. This is achieved in a smooth manner by defining a pressure based switch,  $\chi_1$ :

$$\chi_1 = \frac{1}{1 + PR \times PR} \quad (2.9)$$

$$PR = \frac{|p_{i,j+1} - p_{i,j}|}{\min(p_{i,j+1}, p_{i,j})} \quad (2.10)$$

and defining the flux at the  $j + 1/2$  face as:

$$G_{j+\frac{1}{2}} = \chi_1 G_{MC} + (1 - \chi_1) G_{SW} \quad (2.11)$$

### 3. Boundary Conditions and Numerical Details

The boundaries may be categorized into the following. At an inflow boundary, the flow vector  $\{\rho, \rho u, \rho v, \rho e\}$  is specified according to the known freestream values. At solid boundaries, the velocity vector and the normal pressure gradient are assumed to be zero and at a constant surface temperature. At outflow boundaries, the flow is assumed predominantly supersonic and the zero gradient extrapolation condition is applied. The boundary conditions for the implicit portion of the algorithm are described in Ref. [35].

The convergence or the absence of it for unsteady calculations is determined by monitoring several quantities. The global residual, defined as:

$$\|G.R.\| = \frac{1}{(IL)(JL)} \sqrt{\sum_{i=1}^{IL} \sum_{j=1}^{JL} \sum_{k=1}^4 \left( \frac{(R_k)_{i,j}}{U_{\infty,k}} \right)^2} \quad (3.1)$$

is a measure representative of the overall solution. In Equation 3.1,  $k$  denotes the  $k^{th}$  component of  $U$  on an  $IL \times JL$  computational mesh and  $(R_k)_{i,j}$  is the change in the flow solution,  $R_k = \Delta U_k$  at  $i, j$  and  $U_{\infty} = \{\rho, \rho u, \rho v, \rho e\}_{\infty}$ . For plotting purposes, these values are normalized by the value of  $\|G.R.\|$  obtained after the first iteration. Convergence is assumed when  $\|G.R.\|$  drops 8 or more orders of magnitude. After this, the surface pressure and heat transfer are monitored over several two characteristic times,  $T_c = L/U_{\infty}$ , where  $U_{\infty}$  is the freestream velocity and  $L$  is a macroscopic length scale – the diameter of the cylinder or the length from the leading edge to the corner. In addition, the integrated root mean square (RMS) pressure and heat transfer values over the entire surface are also monitored. With  $P$  and  $Q$  denoting pressure and heat transfer respectively:

$$(P)_{RMS} = \frac{1}{IL} \sqrt{\sum_{i=1}^{IL} \left( \frac{p_{i,j=surface}}{p_{\infty}} \right)^2} \quad (3.2)$$

$$(Q)_{RMS} = \frac{1}{IL} \sqrt{\sum_{i=1}^{IL} (Q_{i,j=surface})^2} \quad (3.3)$$



## 4. Results

The parameters for this flow are chosen after consideration of available experimental data from Wieting *et al.* [5]:  $M_\infty = 8.03$ , Cylinder Radius = 1.5in.,  $T_\infty = 200.8R$  and  $T_{\text{wall}} = 530R$ . The impinging shock angle is  $18.1^\circ$  corresponding to a post-shock Mach number of 5.25. The experimental results were reanalyzed and published by Thareja *et al.* [15] who also performed a computational study in which they varied the impinging shock location to obtain the best fit with experimental data. From their work, we choose the reference point for the impinging shock as  $(-3.5/1.5R, -0.522/1.5R)$  where  $R$  is the radius and the point  $(0,0)$  corresponds to the cylinder center. This is denoted as Case S0 in Ref. [15].

Figure 2 illustrates the general features of the mesh employed. The inflow computational boundary is assumed to be a sequence of piecewise smooth spirals bounding the domain of interest. In the radial direction the grids are stretched algebraically. Three grids are employed in this study with the coarser meshes (Grids 1 and 2) being extracted systematically from the finest mesh (Grid 3) in a multigrid fashion. The salient characteristics of each grid are presented in Table 1.

In the coarse mesh calculation the basic features of the flow structure are reproduced (Figure 3). However, the shock system exhibits significant staircasing and the details of the supersonic jet and the bounding shear layers are not discernible. One interesting aspect of the calculation is the dependence of the final solution upon the time step size utilized. At low time steps, an unsteadiness is evident in the global residual criterion and, to a lesser extent, in the aggregate surface quantities (RMS pressure and heat transfer). On the other hand, at larger time step sizes, the solution converges to machine accuracy. Preliminary calculations with both the van Leer and Roe methods exhibit unsteady limit cycles in each of the monitored quantities at all achievable time-step sizes. The employment of characteristic boundary conditions on the outflow boundaries has no effect upon these

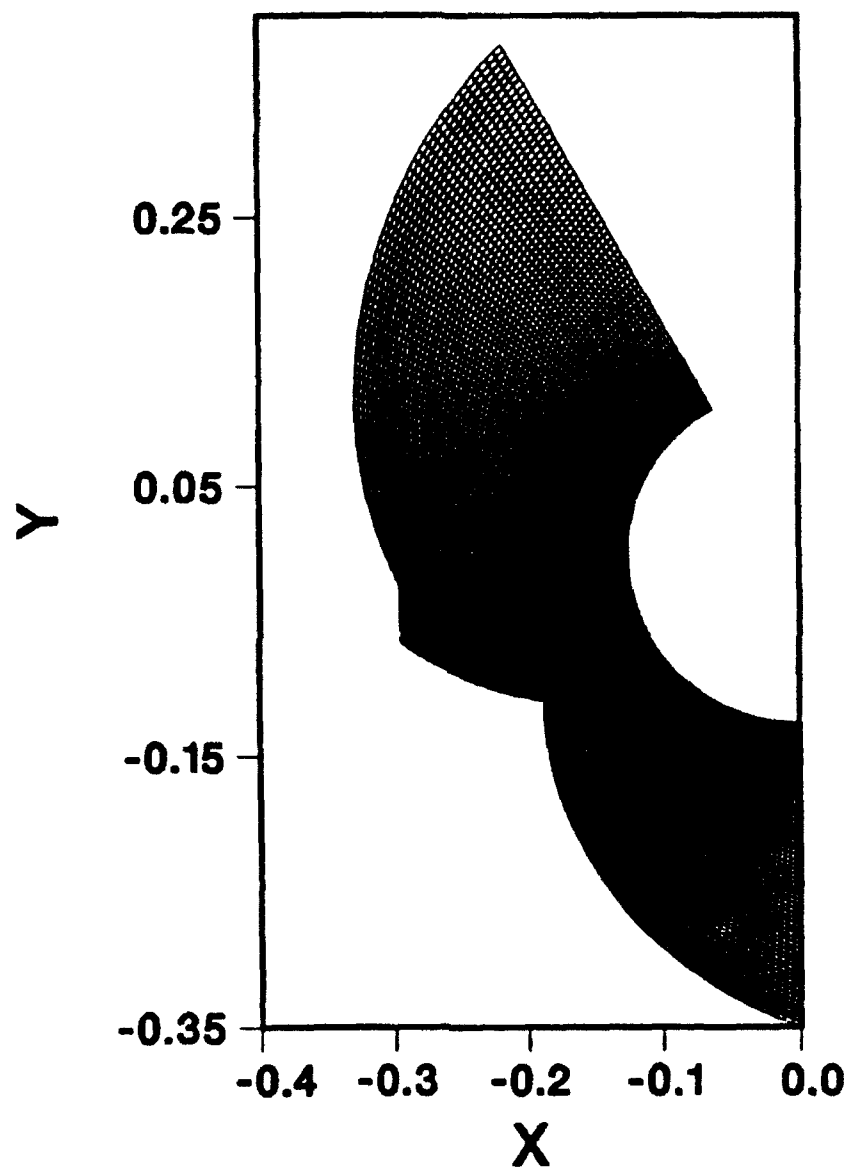


Figure 2: Structure of grid employed

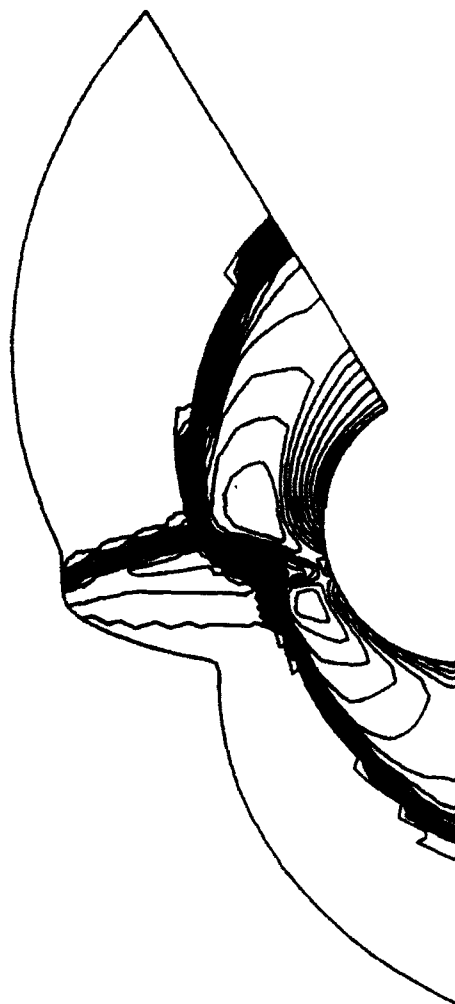


Figure 3: Mach contours on coarse mesh

Table 1: Shock Interference Grid Details

Grid	$IL \times JL$	$Re_c _{min}$	$Re_c _{max}$	$Re_c _{av}$	$\Delta\theta _{min}$	$\Delta\theta _{max}$	$\Delta\theta _{av}$	$c _{av}$
1	$49 \times 24$	5.6	17.9	10.4	1.8	4.0	3.1	2.0
2	$99 \times 49$	2.2	7.5	4.3	0.9	2.0	1.5	1.4
3	$199 \times 99$	1.0	3.4	2.0	0.45	1.0	0.8	1.2

Legend:  $IL$  - Points in  $\xi$  direction  $JL$  - Points in  $\eta$  direction  
 $Re_c$  - Surface mesh Reynolds number  $\Delta\theta$  - Angular spacing (deg)  
 $c$  - Stretch factor at surface  
Subscripts:  $av$  - average  $min$  - minimum  
 $max$  - maximum

limit cycles which are described in more detail below.

The apparent contradiction in the asymptotic behavior among the three algorithms (MC, van Leer and Roe) is examined further with reference to the numerical method. For problems with steady-state solutions, the code is typically operated at the highest achievable inviscid CFL number. The MC scheme is most robust in this regard. Operational CFL numbers between 1000 – 5000 are achieved with the higher number pertaining to the coarser meshes. In contrast, achievable CFL numbers with Roe's scheme are an order of magnitude lower while the van Leer scheme is the least robust ( $CFL < 25$ ). It is known that at high time-step sizes and with a fixed number of sweeps, the Gauss-Seidel algorithm exhibits maximal damping [30] indicating the possibility of false steady results with higher  $\Delta t$  values. On the other hand, Yee *et al.* [36] state that "discrete maps" of nonlinear equations can produce solutions which do not satisfy the original continuous system. Such solutions can manifest themselves as spurious, unsteady cycles of any period, and may be

obtained at time step sizes above or sometimes even below the linearized stability limit. They suggest that unsteady asymptotic behavior be examined in the limit  $n \rightarrow \infty$ ,  $\Delta t \rightarrow 0$  where  $n$  is the number of iterations.

The time accuracy of the present code is first investigated on the intermediate mesh. The discretization utilized is based on the Euler implicit formula and is, therefore, formally first-order time accurate. The solution procedure, Gauss-Seidel line relaxation, may be viewed as time accurate within the framework of the sub-iteration strategy [28]. Nevertheless, the use of inconsistent differencing (through the use of Steger Warming Jacobians) on the left hand *NUMERICS* portion is relevant to this issue and a detailed examination is performed in the limit  $\Delta t \rightarrow 0$  by a combination of increased number of sweeps per iteration (from two to four) and a reduction in  $\Delta t$ . At each time-step, therefore, the equations are solved to within a certain tolerance. A consistent strategy of reducing  $\Delta t$  is followed until the results, monitored with the above mentioned aggregate and local quantities, are independent of  $\Delta t$ . The assumption that the limit cycle is independent of the initial conditions is implied and tested by starting the solution from a converged blunt body shock and separately from a uniform flow condition. The time-step size independent limit cycles in both instances are identical.

The process outlined above is discussed with reference to Grid 2. A limit cycle is first obtained with a relatively high but constant  $\Delta t$ , corresponding to a CFL number varying slightly about 4000. The time-step is successively halved and the solution marched until a new limit cycle is reached. This process is halted when halving  $\Delta t$  has no perceptible influence upon the limit cycle as reflected on several aggregate and local quantities. The results are shown in Figure 4(a) for the quantity  $\log(||GR||)$  of Equation 3.1. The extreme values in the residual exhibit a four-period type of oscillation. Although the profiles of the other quantities monitored are different, the influence of time-step reduction is similar. The initial reductions in  $\Delta t$  result in an increase in amplitude of oscillation. Below  $\Delta t = 0.003T_c$ ,

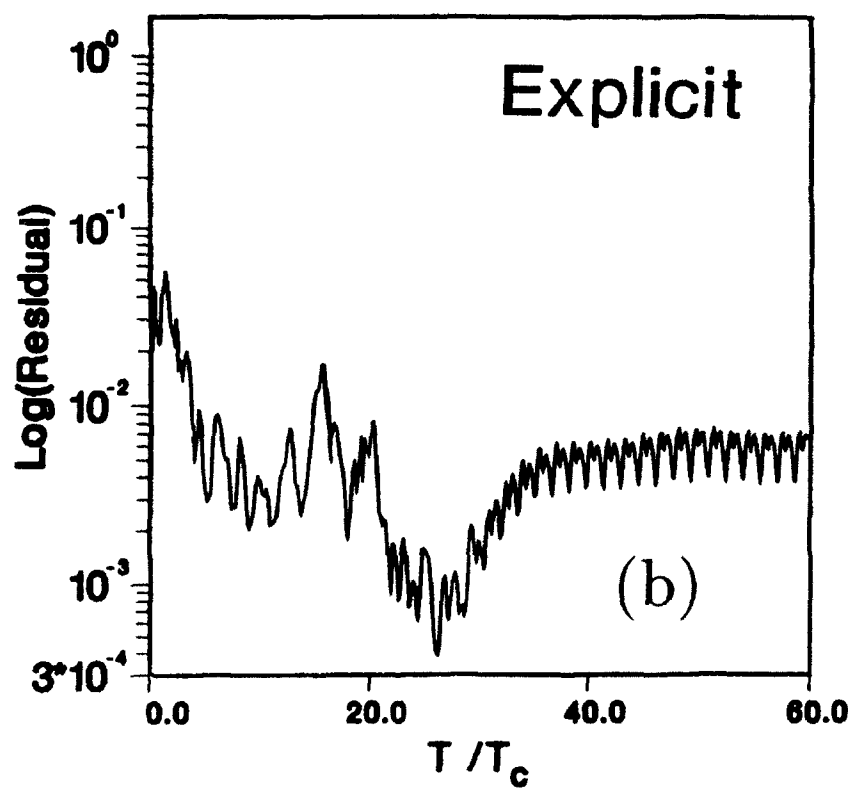
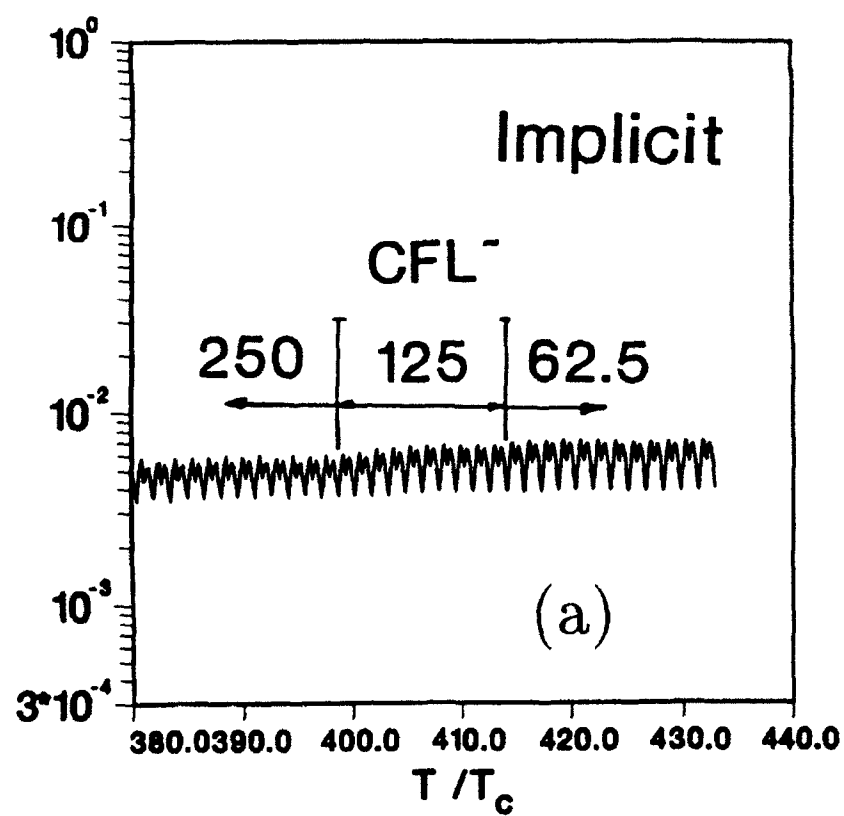


Figure 4: Log residuals on Grid 2 Type IV interaction

corresponding to a CFL number of about 125, no further influence of reduction is observed. The implicit solution is compared with results from an explicit second order time and space accurate method – a two-step predictor corrector algorithm (Heun's scheme). This method yields time-step size independent results at the linearized stability limit ( $CFL \sim 0.9$ ). The entire  $\log(||GR||)$  history of the explicit algorithm is shown in Figure 4(b).

Results from the explicit and implicit algorithm are compared in Figure 5 for several quantities monitored over one cycle spanning the dominant frequency. In these figures, the profiles from the explicit calculation are translated along the time axis until they match the implicit time development. The displayed quantities are the aggregate quantities: global residual, the instantaneous RMS surface pressure and heat transfer over the entire surface and the local quantities: maximum surface pressure and heat transfer which occur in the vicinity of the location of the impinging jet. It is clear that the error in amplitude and frequency between the implicit and explicit methods is negligible for all quantities monitored. Indeed, the largest discrepancy occurs in the maximum heat transfer rate on the surface where the relative error is only 0.1%. Although the unsteadiness in this computation is evident in the aggregate quantities presented, the variation of local quantities is not pronounced. For example, the difference between the peak and trough in the maximum heat transfer cycle is only 2% of the mean while that for pressure is 1.25%. The detailed flow features reveal only a modest degree of unsteadiness in the overall flow structure.

The unsteady features are more apparent in results obtained on Grid 3. These results were obtained at  $\Delta t = 0.001T_c$ . Figure 6 displays the computed limit cycles of the  $\log(||GR||)$  and maximum pressure and maximum heat transfer, respectively. The basic four-period type oscillation similar to that observed on Grid 2 is discernible although the regularity does not persist. The range of values obtained by the maximum heat transfer and pressure is much larger, however (65% and 30% about the mean, respectively). A spectral analysis of these limit cycles reveals a dominant frequency of about 32kHz. In

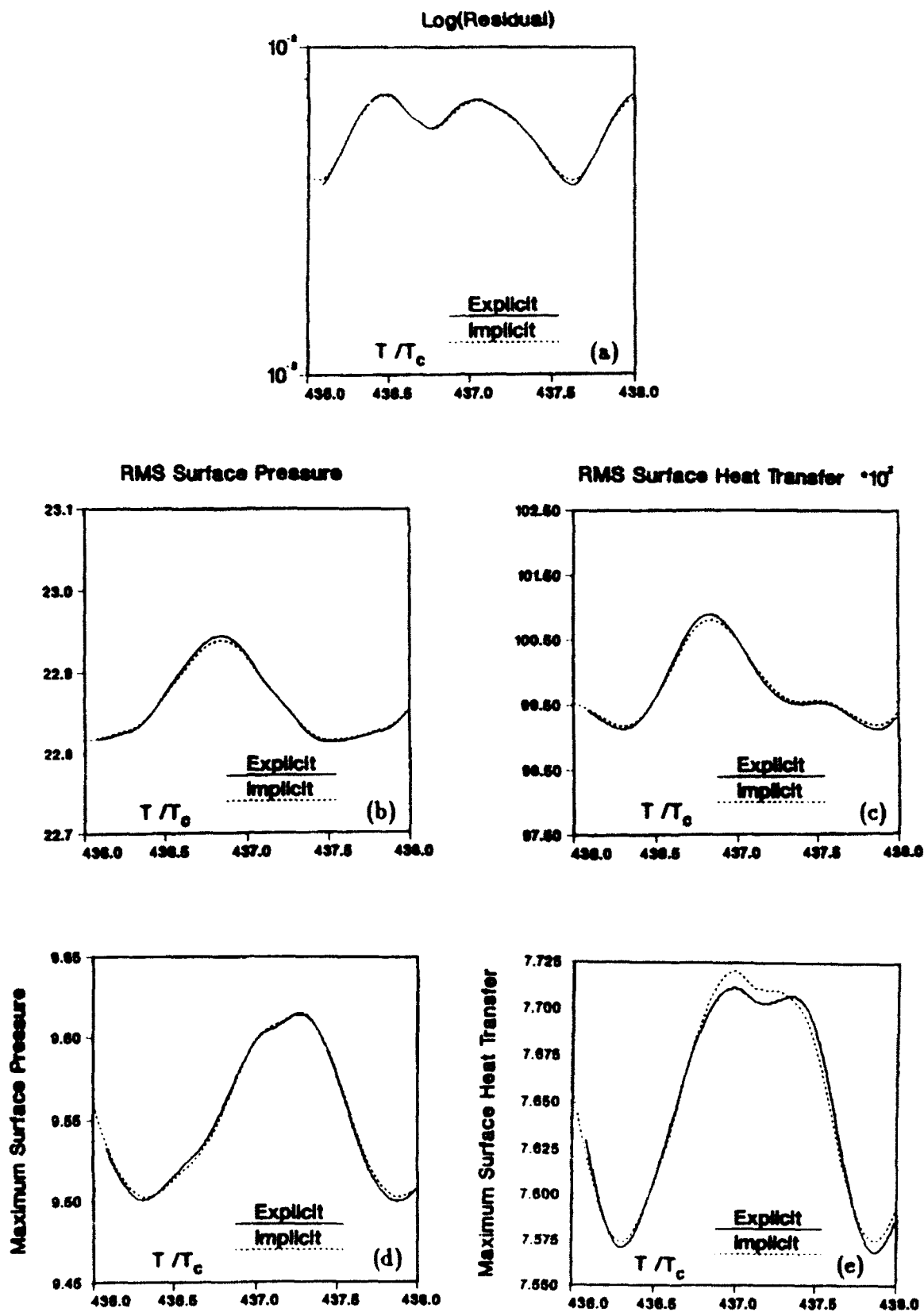


Figure 5: Comparison of implicit and explicit algorithm time histories on Grid 2 - Type IV interference



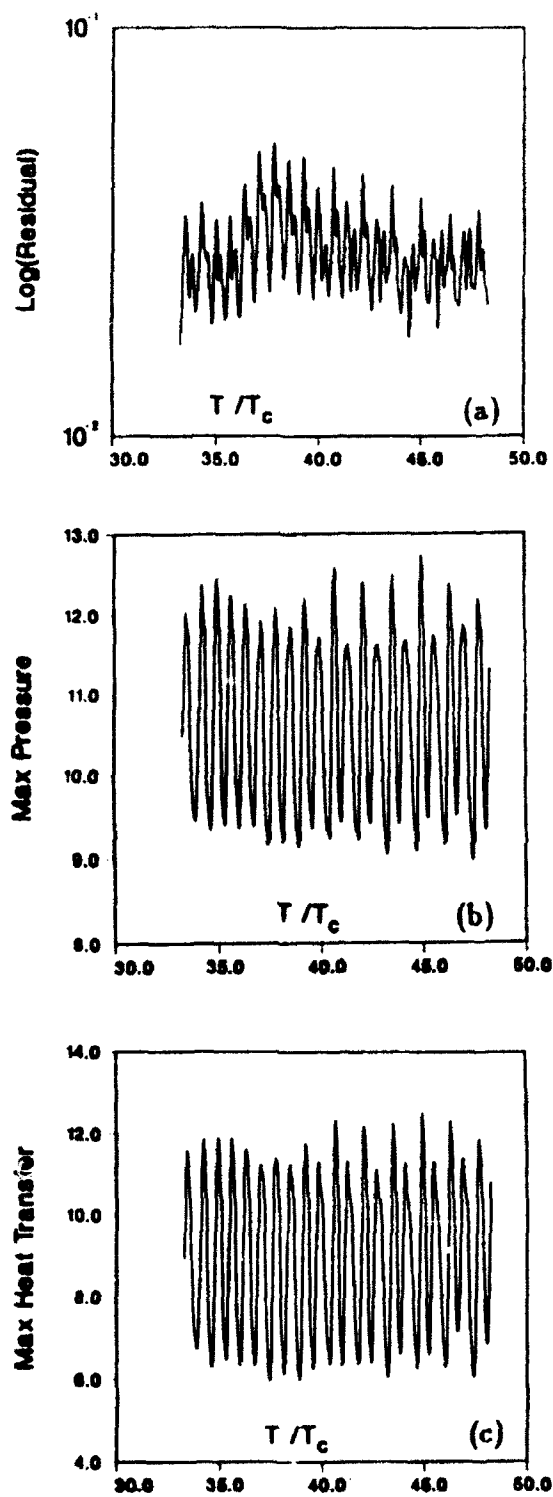


Figure 6: Time history of Type IV interaction on Grid 3

comparison, the experimentally observed frequencies for Type IV interactions are in the range of 3 to 10kHz [16]. An estimate of the frequency supportable by Mesh 3 may be based on a wavelength of  $2\Delta x$  and a sonic wave speed in the stagnation region. Choosing  $\Delta x$  as the grid spacing in the circumferential direction, the resolvable frequency (1080kHz) is much higher than that observed in the present physical phenomenon. The number of time-steps within each cycle is about 800.

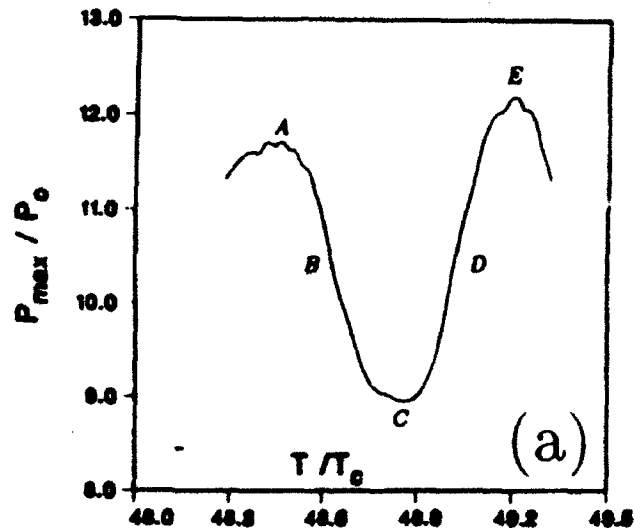
A small portion of the residual cycle spanning two consecutive crests of maximum pressure representing the dominant frequency is isolated for further study (Figure 7(a)). The maximum heat transfer cycle is shown in Figure 7(b). The time between the two pressure peaks is  $0.75T_c$  corresponding to a frequency of  $30kHz$ . The maximum heat transfer is similar to the peak pressure with a small leading phase.

Five points denoted  $A, B, C, D$  and  $E$  are identified on the pressure profile between the two successive peaks. The Mach contours at these points are shown in Figure 8. The distorted bow shock as well as the impinging shock are captured within at most two zones. The shear layers emanating from the two triple points are also well resolved. However, some portions of the distorted bow shock exhibit the "zig-zag" phenomenon which can result in a degradation of accuracy [37].

The most significant difference in the Mach patterns appears to be the angle made by the terminating jet shock with the surface of the cylinder. This shock oscillates about two positions. At one extreme (location  $A$ ) it forms an acute angle with the surface tangent of the cylinder at the stagnation point. At the other extreme (location  $C$ ), the terminating jet shock is parallel to the cylinder surface tangent. This shock movement is accompanied by changes in the angle with which the supersonic jet between the two shear layers impinges upon the body surface.

The surface pressure and heat transfer corresponding to the points  $A$  through  $E$  are exhibited in Figure 9. The pressure is normalized by the stagnation pressure obtained with

## Surface pressure



## Heat transfer

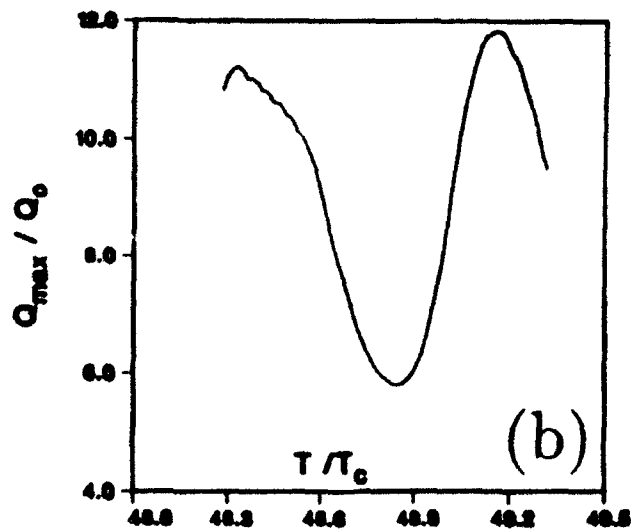


Figure 7: Representative maximum surface loading cycles - Grid 3 Type IV interaction

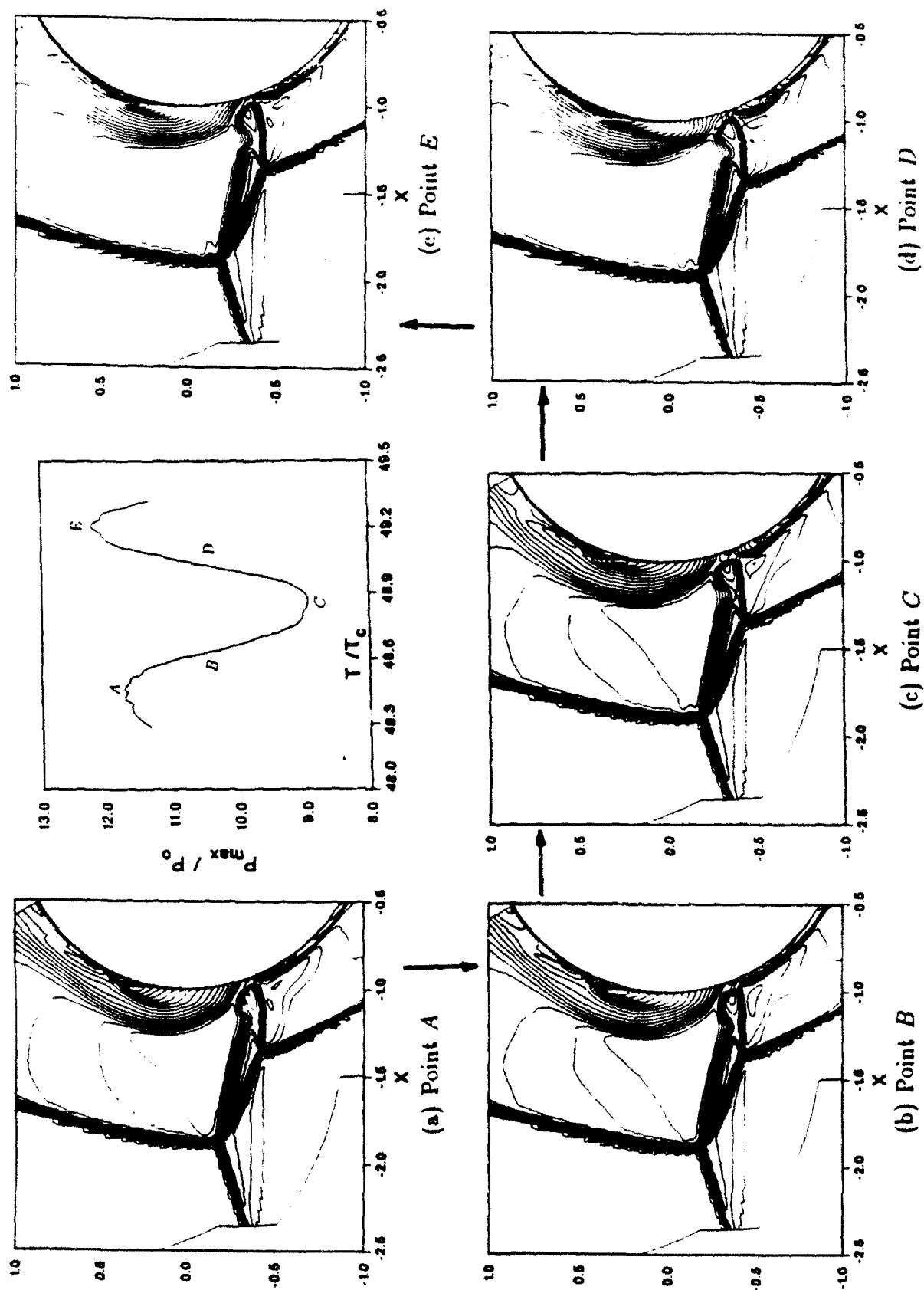


Figure 8: Mach contours at various points in limit cycle - Grid 3 Type IV  
interaction

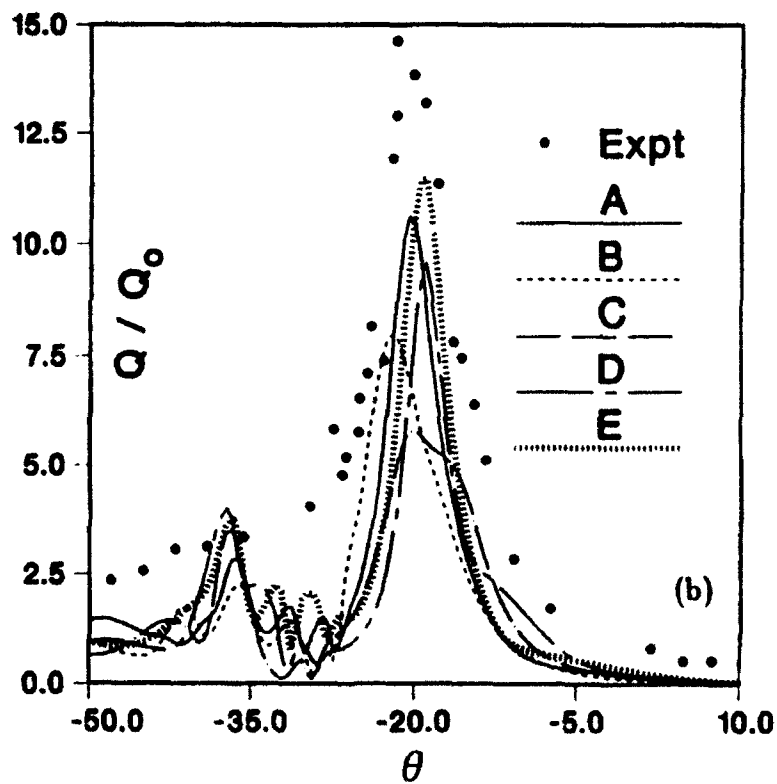
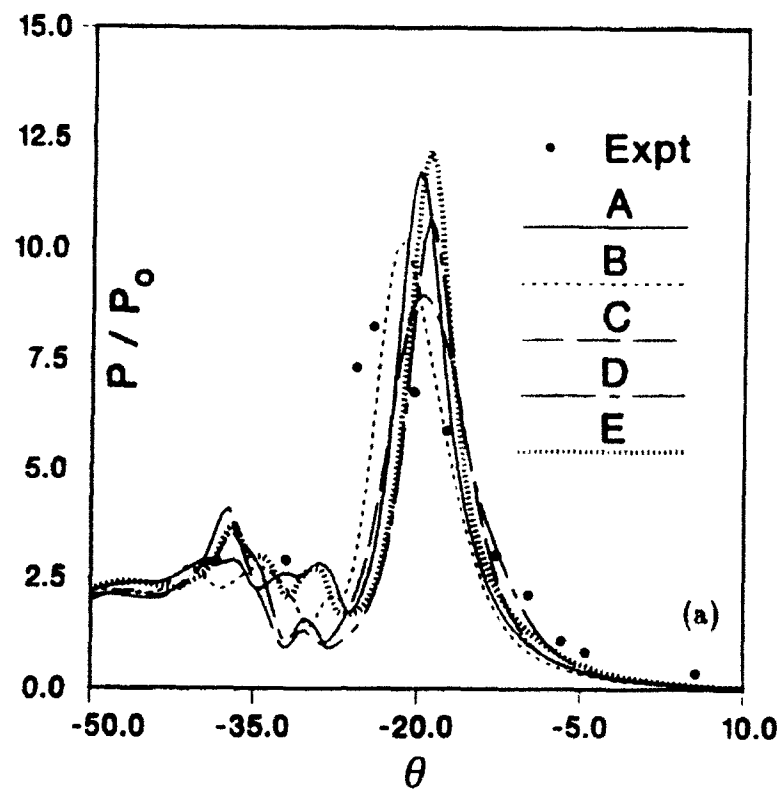


Figure 9: Surface loading at various points in limit cycle - Grid 3 Type IV interaction

the Rayleigh formula. For heat transfer normalization, we follow the approach of Thareja *et al.* [15]. Although the experimental noninterfering stagnation heat transfer value is  $61.7 \text{ Btu/ft}^2 - \text{sec}$ , they argue that since the theoretical value for peak heat transfer, obtained with a VSL (Viscous Shear Layer) analysis is  $41.43 \text{ Btu/ft}^2 - \text{sec}$ , the difference may be factored out by utilizing the higher (61.7) value to normalize experimental results and the lower value (41.43) for computed values. The abscissa,  $\theta$ , is the angle measured with respect to the horizontal, negative values denoting the cylinder surface below the noninterfering stagnation streamline (Figure 8). At point *A*, the first peak of the pressure cycle, the terminating jet points upward and the corresponding maximum pressure occurs at  $\theta \sim -18.5^\circ$ . Between points *A* and *B*, the terminating jet shock assumes a position parallel to the surface tangent and remains so until after point *C*. During this time, the maximum surface pressure location moves downward to a position of  $\theta \sim -21^\circ$  and the terminating jet impinges more perpendicularly to the surface than at point *A*. Between points *C* and *D*, the terminating jet shock again assumes a position similar to that at point *A* and remains in this position until point *E*. Correspondingly the maximum surface pressure point moves upwards until it reaches a maximum of  $-18.2^\circ$ . The temporal development of the surface heat transfer is generally similar to that of the surface pressure in phase and location. After point *E*, the cycle repeats in the qualitative features though the peak values obtained differ by a modest amount between various cycles.

Overall, the computed surface pressure overpredicts the experimental observations. The computed location of the maximum pressure oscillates  $\Delta\theta \sim 2.5^\circ$  about a mean at  $\theta \sim -20^\circ$ . The best agreement in magnitude of the pressure peak is obtained at point *C* on the limit cycle (6% overpredicted). However, the location of this peak ( $-19.5^\circ$ ) is about  $4.5^\circ$  above the experimental value ( $-24^\circ$ ). The maximum discrepancy in peak pressure is at point *E*.

In contrast to the surface pressure, the heat transfer is underpredicted at all points in

the limit cycle. One explanation is based on the fact that the impinging supersonic jet is processed through several oblique shocks and expansion fans. In this region, the effect of the switching mechanism reverting the MC scheme to the SW scheme is not clear and may influence the quantitative calculations in the surface quantities. Inadequate grid resolution may be another factor. The lowest value of peak heat transfer occurs at point *C* while the highest value (underpredicted by 20%) occurs at point *E*. The locations of the heat transfer peaks fall roughly within the experimental envelope. In the lower portion of the cylinder, in the region between  $-25^\circ$  and  $-45^\circ$ , both the surface pressure and heat transfer distributions exhibit spatial as well as temporal oscillations. The heat transfer in this region as well as on the upper portion of the cylinder is underpredicted. This is similar to the overall observations of other researchers [12].

Further examination of the computed flowfield reveals the existence of two distinct regions of unsteady separation, one below the jet impingement position ( $-35^\circ$  to  $-29^\circ$ ) and the other above ( $24^\circ$  to  $35^\circ$ ). The lower separated flow is in the vicinity of the region where the surface pressure and heat transfer were seen to exhibit spatial oscillations. The angular extent of this separation region, monitored with the skin friction coefficient, fluctuates in time. The second separation region, above the stagnation point, is caused by a recompression experienced by the flow as it rounds the upper portion of the cylinder. This compression results in a pressure rise on the surface causing boundary layer separation.

It should be noted that in previous research with the Euler equations [18], a recompression shock system was observed in clear detail on the upper portion of the cylinder. The surface Mach number near the point of impingement of the compression shock was higher than unity. This is precluded in the present research by the viscous boundary conditions. The inviscid results of Ref. [18] for the same interaction with the Roe as well as with the "Upwind" TVD schemes also indicate an oscillating surface pressure profile. In that calculation, however, the point in the cycle where the jet terminates normal to the surface (e.g.,

point *C* above) results in the highest pressure peak in contrast to the present behavior. One possible explanation for this difference is based upon the influence of dissipation upon the strength and location of the terminating jet shock. At point *C* in the limit cycle, the jet shock is nearly parallel to and farther away from the surface than at point *A* where the shock is somewhat oblique to the flow. In the viscous stagnation region, the dissipation mechanism (whether numerical or physical) not only alters the total pressure and temperature recovery based upon shock strength but may also change the information propagation characteristics. This mechanism could introduce a phase lag between the shock system and the corresponding surface effects.

The source of the unsteadiness observed in the computation is not clear. The numerical aspect of the solution has not been fully examined in the context of spatial and temporal accuracy. The physical mechanisms acting upon the triple-point and the flow properties of the shear layers bounding the supersonic jet are complex. In addition the shear layers are subject to inviscid instability and, depending upon the Reynolds number in the adjacent shock layer, transition to turbulence can occur [16]. Further work is required to resolve these issues.



## 5. Conclusions

Results for the Type IV interaction display unsteady flow behavior with all three algorithms. A study of the computed unsteady flow field has been performed with the MC scheme. A large scale movement of the supersonic impinging jet is observed with accompanying influences on the remainder of the flow. The dominant frequency of the observed phenomenon is about 32 kHz on the finest mesh. Unsteady separation regions are observed both above and below the point of jet impingement. Surface pressures show modest discrepancies with experiment while heat transfer rates are underpredicted.

## 6. References

- [1] Committee on Hypersonic Technology for Military Application. Hypersonic Technology for Military Applications. Technical report, National Academic Press, Washington, D.C, 1989.
- [2] B. Edney. Anomalous Heat Transfer and Pressure Distributions on Blunt Bodies at Hypersonic Speeds in the Presence of an Impinging Shock. Technical Report 115. The Aeronautical Research Institute of Sweden, Stockholm, February 1968.
- [3] R. Craig and P. Ortwerth. Experimental Study of Shock Impingement on a Blunt Leading Edge with Application to Hypersonic Inlet Design. Technical Report TR-71-10, AFAPL, October 1971.
- [4] M.S. Holden, A.R. Wieting, J.R. Moselle, and C. Glass. Studies of Aerothermal Loads Generated in Regions of Shock/Shock Interaction in Hypersonic Flow. *AIAA Paper 88-0477*, 1988.
- [5] A.R. Wieting and M.S. Holden. Experimental Study of Shock Wave Interference Heating on a Cylindrical Leading Edge at Mach 6 and 8. *AIAA Paper 87-1511*, 1987.
- [6] F.D. Hains and J.W. Keyes. Shock Interference Heating in Hypersonic Flows. *AIAA Journal*, 10(11):1441-1447, November 1972.
- [7] D.J. Morris and J.W. Keyes. Computer Programs For Predicting Supersonic and Hypersonic Interference Flow Fields and Heating. Technical Report TM X-2725, NASA, May 1973.
- [8] D.H. Crawford. A Graphical Method for the Investigation of Shock Interference Phenomena. *AIAA Journal*, 11(11):1590-1592, November 1973.

- [9] T.T. Bramlette. Simple Technique for Predicting Type III and Type IV Shock Interference. *AIAA Journal*, 12(8):1151-1152, August 1974.
- [10] J. Tannehill, T. Holst, J. Rakich, and J. Keyes. Comparison of a Two-Dimensional Shock Impingement Computation with Experiment. *AIAA Journal*, 14(4), April 1976.
- [11] J.A. White and C.M. Rhie. Numerical Analysis of Peak Heat Transfer Rates for Hypersonic Flow Over a Cowl Leading Edge. *AIAA Paper 87-1895*, 1987.
- [12] G.H. Klopfer and H.C. Yee. Viscous Hypersonic Shock-On-Shock Interaction on Blunt Cowl Lips. *AIAA Paper 88-0233*, 1988.
- [13] K.M. Peery and S.T. Imlay. Blunt-Body Flow Simulations. *AIAA Paper 88-2904*, 1988.
- [14] Y.J. Moon and M. Holt. Interaction of an Oblique Shock Wave with Turbulent Hypersonic Blunt Body Flows. *AIAA Paper 89-0272*, 1989.
- [15] R.R. Thareja, J.R. Stewart, O. Hassan, K. Morgan, and J. Peraire. A Point Implicit Unstructured Grid Solver for the Euler and Navier-Stokes Equations. *International Journal for Numerical Methods in Fluids*, 1989.
- [16] M.S. Holden. Shock-Shock Boundary Layer Interactions. *AGARD Report 764. Special Course on Three-Dimensional Supersonic/Hypersonic Flows Including Separation*, 1990.
- [17] R.K. Prabhu, J.R. Stewart, and R.R. Thareja. Shock Interference Studies on a Circular Cylinder at Mach 16. *AIAA Paper 90-0606*, 1990.
- [18] N. Kroll, D. Gaitonde, and M. Aftosmis. A Systematic Comparative Study of Several High Resolution Schemes for Complex Problems In High Speed Flows. *AIAA Paper 91-0636*, 1991.

- [19] R. MacCormack. The Effect of Viscosity in Hypervelocity Impact Cratering. *AIAA Paper 69-0354*, 1969.
- [20] R.F. Warming and R.M. Beam. Upwind Second-Order Difference Schemes and Applications in Aerodynamic Flows. *AIAA Journal*, 14(9):1241-1249, September 1976.
- [21] A. Jameson, W. Schmidt, and E. Turkel. Numerical Solutions of the Euler Equations by a Finite Volume Method Using Runge-Kutta Time Stepping Schemes. *AIAA Paper 81-1259*, 1981.
- [22] J.L. Steger and R.F. Warming. Flux Vector Splitting of the Inviscid Gasdynamic Equations with Application to Finite Difference Methods. *Journal of Computational Physics*, 40(2):263-293, April 1981.
- [23] B. van Leer. Flux-Vector Splitting For the Euler Equations. Technical Report 82-30. ICASE, September 1982.
- [24] P.L. Roe. Approximate Riemann Solvers, Parameter Vectors and Difference Schemes. *Journal of Computational Physics*, 43:357-372, 1981.
- [25] H.C. Yee. Construction of Implicit and Explicit Symmetric TVD Schemes and Their Applications. *Journal of Computational Physics*, 68:151-179, 1987.
- [26] H.C. Yee and A. Harten. Implicit TVD Schemes for Hyperbolic Conservation Laws in Curvilinear Coordinates. *AIAA Journal*, 25:266-274, 1987.
- [27] R.W. MacCormack and G.V. Candler. The Solution of the Navier-Stokes Equations with Gauss-Seidel Line Relaxation. *Symposium in Honor of G. Moretti's 70th Birthday*, 1987.
- [28] J.L. Thomas, B. van Leer, and R.W. Walters. Implicit Flux-Split Schemes for the Euler Equations. *AIAA Paper 85-1680*, 1985.

- [29] R. MacCormack. Current Status of Numerical Solutions of the Navier-Stokes Equations. *AIAA Paper 85-0032*, 1985.
- [30] J.L. Thomas and R.W. Walters. Upwind Relaxation Algorithms for the Navier Stokes Equations. *AIAA Paper 85-1501CP*, 1985. Also, *AIAA J.*, Vol.25, No. 4, April, 1987.
- [31] W.K. Anderson, J.L. Thomas, and B. van Leer. A Comparison of Finite Volume Flux Vector Splittings for the Euler Equations. *AIAA Paper 85-0122*, 1985.
- [32] B. van Leer. Towards the Ultimate Conservation Difference Scheme V. A Second-Order Sequel to Godunov's Method. *Journal of Computational Physics*, 32:101-136, 1979.
- [33] H.C. Yee, G.H. Klopfer, and J.-L. Montagne. High-Resolution Shock-Capturing Schemes for Inviscid and Viscous Hypersonic Flows. Technical Report 100097, NASA - Ames Research Center, Moffet Field, California, April 1988.
- [34] R.W. MacCormack and G.V. Candler. The Solution of the Navier-Stokes Equations Using Gauss-Seidel Line Relaxation. *Computers & Fluids*, 17(1):135-150, 1989.
- [35] D. Gaitonde and J. Shang. A Numerical Study of Viscous Shock-on-Shock Hypersonic Flows with a Modified Steger-Warming Flux Split Scheme. *AIAA Paper 90-1491*, 1990.
- [36] H.C. Yee, P.K. Sweby, and D.F. Griffiths. A Study of Spurious Asymptotic Numerical Solutions of Nonlinear Differential Equations by the Nonlinear Dynamics Approach. *Lecture Notes in Physics, Twelfth International Conference on Numerical Methods in Fluid Dynamics*, 371:259-267, 1990.
- [37] B. Müller. Simple Improvements of an Upwind TVD Scheme for Hypersonic Flow. *AIAA Paper 89-1977-CP*, 1989.

## Nomenclature

$B$	flux Jacobian of $G$
$Btu$	British Thermal Unit
$c$	stretch factor; local speed of sound
$C_v$	specific heat at constant volume
$CFL$	Courant-Friedrich-Levy number
$e$	total energy
$e_i$	internal energy
$f$	feet
$F, \hat{F}, G, \hat{G}$	flux vectors
$G.R.$	global residual
$IL, JL$	points in $\xi$ and $\eta$ direction
$J$	Jacobian, inverse cell volume
$M$	Mach number
$MC$	MacCormack and Candler scheme
$SW$	Original Steger Warming scheme
$p$	pressure
$psi$	pounds per square inch
$Pr$	Prandtl number
$PR$	pressure function
$Q$	matrix diagonalizing $A$ ; heat transfer
$R$	gas constant; Rankine
$Re$	Reynolds number
$RMSP$	root mean square surface pressure

$RMSQ$	root mean square surface heat transfer
$t$	time
$T$	temperature
$T_c$	characteristic time
$u$	Cartesian velocity in $x$ direction
$U, \hat{U}$	solution vector
$v$	Cartesian velocity in $y$ direction
$\vec{v}$	Cartesian velocity vector
$VSL$	Viscous Shear Layer analysis
$W$	vector of extrapolated variables
$x, y$	Cartesian coordinates
$\delta$	cutoff value; any change
$\Delta$	change across interface
$\tilde{\delta}$	cutoff parameter
$\nabla$	gradient operator
$\gamma$	ratio of specific heats
$\lambda$	eigenvalue
$\Lambda$	eigenvalue matrix
$\partial$	partial derivative operator
$\rho$	density
$\theta$	angle
$\xi, \eta$	transformed coordinates

$X_i$  pressure switch

### Subscripts

$j + \frac{1}{2}$  interface between cells  $j$  and  $j + 1$

$v$  viscous

$w$  wall

$\infty$  freestream conditions

### Superscripts

$L$  state at left of interface

$R$  state at right of interface

$+, -$  positive and negative components